Impact Dynamics of Droplet Containing Particle Suspensions on Deep Liquid Pool

Boqian Yan¹ and Xiaoyu Tang¹*

¹Department of Mechanical and Industrial Engineering, Northeastern University, Boston, USA, 02115.

*Corresponding author. Email: x.tang@northeastern.edu

Abstract

Droplet impact on surfaces is ubiquitous in many natural and industrial processes. While the impact dynamics of droplets composed of simple fluids have been studied extensively, droplets containing particles are less explored, but are more application relevant. The non-Newtonian behavior of particle suspension introduces new physics affecting the impact dynamics. Here, we investigated the impact dynamics of droplets containing cornstarch particles on a deep water pool and systematically characterized the impact outcomes with various Weber number and particle volume fractions. Distinctive phenomena compared to Newtonian droplet impact have been observed. A regime map of the impact outcomes is unveiled and the transition boundaries are quantified with scaling analysis. Rheology of the suspension is found to play a pivotal role in giving rise to distinct impact outcomes. The results lay the foundation for further characterization of the dynamics of suspension droplet impacting on liquid surfaces and can be translated to other suspension fluids.

Keywords: Drop impact; Non-colloidal suspension; Shear thickening; Complex fluids; Jamming; Soft matter.

1 Introduction

Droplet impact on surfaces [1–12] is important in engineering and manufacturing industries, such as spray coating [13], inkjet printing [14], and fuel injection in combustion systems [15]. Controlling the droplet impact dynamics enables engineers to manipulate mass transfer rates, enhance mixing efficiency, and optimize the yield and quality of desired products. The droplet impact process is orchestrated by the interplay of inertial, viscous, and capillary effects, giving rise to a variety of intriguing outcomes, such as bouncing [16–21], spreading [22–27], splashing [28–34], and bubble entrapment [35–37]. Various studies have been performed to unveil the controlling physics to quantify the dynamics such as spreading diameter [22–27], splashing criteria [28–34, 38], and interstitial layer dynamics [39–41]. Summary of these studies can be found in review papers by [1, 42].

Most of these studies are predominantly focused on droplets of simple liquids such as water and oil. However, complex fluids that contain colloidal particles are more common in applications such as coating and printing. When a droplet contains colloidal particles, non-Newtonian behaviors [43–45] including shear thinning, shear thickening, and shear jamming become apparent, adding another layer of complexity to the impact dynamics. Specifically, the viscosity of the droplet is dependent on the shear rate, which changes both temporally and spatially during the impact process, leading to time-dependent and nonhomogenous viscous effect. On the other hand, the impact-induced flow field redistributes the particles, which may also go through non-equilibrium states [46, 47], further leading to heterogeneous viscosity distribution. Consequently, the interplay between particle distribution and impact dynamics gives rise to interesting physics for impact of suspension droplet on surfaces.

Distinctive outcomes and dynamics have been observed for the impact of suspension droplets on solid substrates[11, 48–51]. Boyer et.al [48] found limited spreading behavior of the droplet which contains colloidal particles with high volume fraction due to shear thickening during the impact process. Moreover, it was observed that

the ultimate deformation of the droplet remains unaffected by variations in the impact velocity. Driscoll [49, 50] tracked the motion of the jamming front and found the occurrence of jamming after a few milliseconds after the droplet contacts the solid surface. Furthermore, they ascertained that the droplet can be effectively modeled by an elastic solid ball, particularly under high volume fraction conditions. Coexistence of liquid and solid phases is also observed and discussed.

The substrate property also plays a critical role in the impact dynamics. The solid substrate provides a strong resistance to the impacting suspension droplets which leads to immediate jamming. On the other hand, when the substrate is highly deformable and even miscible with the impacting droplet, the impact dynamics is even more complicated. Specifically, the liquid surface can deform and adapt to the motion of the impact, resulting in a weaker resistant force and reduced spreading of the droplets. This raises the question of whether the droplet still jams during impact on a liquid surface and what new phenomena can be observed.

However, there are limited studies on the dynamics of suspension droplets impacting a liquid surface. Here, we present a systematic experimental study of droplets containing non-colloidal suspension impacting a deep liquid pool to explore the effect of inertia, capillary and rheology on the impact dynamics. Various impact outcomes are observed, some of which are unique to the non-Newtonian system, and are mapped in a regime map in the Weber number (We)-volume fraction (ϕ) space. We captures the effect of inertia and surface tension, while ϕ captures the rheological behavior of particle suspension. We unveiled the controlling physics for each phenomenon and quantified the transition boundaries using scaling analysis.

The paper is organized as follows: In Section 2, we introduce the experimental setup and discuss important parameters, such as the rheology of the cornstarch suspension. In Section 3, we present different phenomena observed in relation to varying volume fractions and impact velocities, and group them into a regime map. We also describe the properties of the cavity and the deformation of the droplet during the

impact process. In Section 4, we use scaling analysis and energy balance model to quantify the transition boundaries between each phenomenon in the regime map.

2 Methodology

2.1 Experimental set-up

Fig. 1 depicts the set-up for the drop impact experiment. Droplet is generated by slowly pushing the liquid through a vertical needle (Gauge 18, McMaster-Carr) using a syringe pump (New Era). Once the weight of the droplet exceeds the surface tension force, the droplet falls assuming a spherical shape. The diameter of the droplet ranges from 2.8 mm to 3.2 mm (see Appendix B). DI water is used as the liquid pool for easy optical access to observe the post impact dynamics inside the pool. The pool is contained in a cubic acrylic chamber with a length of 50 mm, which minimizes the influence of the chamber walls. The impact velocity of the droplet is controlled by adjusting the height between the needle and the liquid surface and ranges from 0.5 m/s to 3.0 m/s. A high-speed camera (Phantom, VEO 1310L) captures side views of the impact dynamics. Front-lighting is used to observe the details of droplet and cavity evolution. MATLAB is used for image post-processing to measure the impact velocity and other features during the impact process.

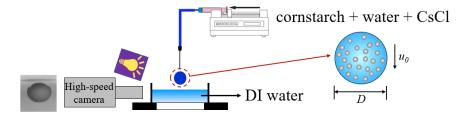


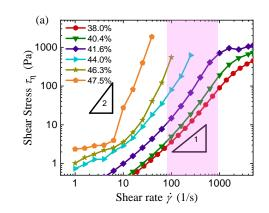
Figure 1: Experimental configuration for studying cornstarch suspension droplet impact on water pool. The diameter of the droplet D and the impact velocity u_0 are measured by image processing.

2.2 Experimental materials and characterization

To prepare the suspension droplets, cornstarch particles (Sigma Aldrich) are mixed with 55 wt.% solution of Cesium Chloride (CsCl) in de-ionized water (DI water). The cornstarch particles are relatively monodisperse and irregularly shaped with a characteristic length of approximately 14 μ m [52]. CsCl is added to enhance particle stability by matching the density of the cornstarch particles $\rho_c = 1630 \text{ kg/m}^3$. The suspension could remain stable for up to one week. Furthermore, since the diameter of particles is larger than 1 μ m, which is referred to as non-colloidal suspension, Brownian motion can be neglected [53]. The volume fraction ϕ of cornstarch particles ranges from 36.8% to 47.5% with an interval of 1.2%, all of which fall below the jamming point. The maximum volume fraction of the cornstarch particles ϕ_{max} at liquid state is tested to be 52.0%. Considering that cornstarch particles are porous, the procedure of calculating volume fraction ϕ follows [54] and is presented in Appendix A.

Rheology of cornstarch suspension of various volume fractions are characterized with a rheometer (TA Instruments, DHR-3), presented in Fig. 2(a). The abrupt stop points at high shear rate for high volume fraction cases in the shear stress τ_{η} - shear strain rate $\dot{\gamma}$ curve are due to jamming, which leads to patches of local solidification and slipperiness, resulting in the stop of the measurements [49]. Typical shear rate during the droplet impact process can be estimated by $\dot{\gamma} = u_0/D$ [48, 49], which ranges from 80 s⁻¹ to 900 s⁻¹ in our experiment, highlighted by the pink shaded region in Fig. 2(a). Shear thickening is observed for all ϕ cases in the experimental shear rate range. The power law $\tau_{\eta} \propto \dot{\gamma}^{\alpha}$ [55] could be further used to categorize the rheological behavior of different volume fractions by extracting the exponent α in the shaded region in Fig. 2(a), and is plotted with respect to ϕ in Fig. 2(b). Since no data is available in the shaded area for $\phi \geq 46.3\%$, α is calculated based on the data points showing obvious shear thickening behavior. The rheological behavior of the cornstarch suspensions can thus be categorized [55] as shown in Table 1 and

marked in Fig. 2(b). Based on this categorization, critical volume fractions of ϕ_{cr1} = 41.0% and ϕ_{cr2} = 45.0% can be identified to group rheological behaviors of cornstarch suspensions into Continuous Shear Thickening (CST), Inertial Transition (IT), and Discontinuous Shear Thickening (DST), as marked in Fig. 2(b). The volume fraction of cornstarch particles plays a critical role in the rheology of the suspension.



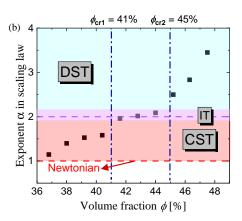


Figure 2: (a) Rheological measurement of cornstarch suspensions with various volume fractions ϕ . Pink shaded area denotes the estimated range of $\dot{\gamma}$ in the experiment, where shear thickening is observed. The slopes of 1 and 2 are for guide of eyes representing Newtonian behavior and discontinuous shear thickening. (b) Variation of exponent α in rheological scaling law $\tau_{\eta} \propto \dot{\gamma}^{\alpha}$ with various volume fractions ϕ . The data is categorized based on the criteria in Table 1. For $\phi \leq 46.3\%$, α is calculated from the data within the pink area. For $\phi \geq 46.3\%$, α is calculated based on the data points showing obvious shear thickening behavior.

Table 1: Rheological categorization of the cornstarch suspension tested in the experiment based on α from scaling $\tau_{\eta} \propto \dot{\gamma}^{\alpha}$ [55].

Ranges of ϕ	Values of α	Properties of fluid
$\phi < 41.0\%$	$1 < \alpha < 2$	Continuous Shear Thickening (CST)
$41.0\% < \phi < 45.0\%$	$\alpha = 2$	Inertial Transition (IT)
$\phi > 45.0\%$	$\alpha > 2$	Discontinuous Shear Thickening (DST)

Surface tension is also important in drop impact dynamics, which is measured by the pendent drop method. Specific details can be found in [56, 57]. The surface

tension of the cornstarch suspension σ_d at different volume fractions ϕ is plotted in Fig. 3. There is no significant change in σ_d with varying ϕ and the values are hovering around the same value as that of DI water marked by the orange dashed line. Thus, $\sigma_d = 72$ mN/m is used as the surface tension of the cornstarch suspension for subsequent analysis and both σ_w , which is the surface tension of the water pool, and σ_d are denoted by σ from here on.

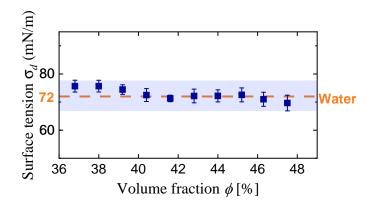


Figure 3: Surface tension measurement of the cornstarch suspension σ_d with various volume fractions ϕ by the pendent drop method. The blue shaded area highlights the range of σ_d with all ϕ . The orange dash line marks the value of surface tension of DI water.

With the experimental materials characterized, the range of relevant non-dimensional numbers can be calculated. In our system of cornstarch suspension droplet impacting on a water pool, the relevant non-dimensional numbers are Weber number $We = \rho_d u_0^2 D/\sigma$ which ranges from 14 – 340 and characterizes the ratio between inertia and surface tension effect, and Reynolds number $Re = \rho_d u_0 D/\eta_d$ which ranges from 1.5 – 300 and characterizes the ratio between inertia and viscous effect. Here, $\rho_d = 1630 \text{ kg/m}^3$ is the droplet density, $\rho_w = 997 \text{ kg/m}^3$ is the density of the pool, and η_d is the viscosity of the droplet. It should be noted that Re is dependent on η_d , which varies with both the impact velocity u_0 and the cornstarch volume fraction ϕ . Moreover, the impact-activated jamming [58, 59] occurs at large u_0 and ϕ , leading to local solidification and rendering the divergence of viscosity.

3 Phenomenology

3.1 Experimental observations

Fig. 4 presents snapshots of the impact process of cornstarch suspension droplets on a water pool at various Weber number We and volume fractions ϕ . At low Weand low ϕ , the droplet merges with the pool, moves down with vortices induced on the side, and eventually detaches from the cavity on the pool surface (Fig. 4(a)), Liquid Lump). The cornstarch particles keep falling down as a coherent mass lump after impacting the water surface. This phenomenon is similar to the impact of dilute suspension droplet on liquid surface [60]. As We increases, the cavity gains more energy to push the mass from the droplet and disperse them, resulting in the mass from the droplet partially attached to the cavity (Fig. 4(b), Partially Attached). The vortices are more pronounced as they interact with the cavity. As We further increases, the cavity has even more energy to expand radially and disperse the mass from the droplet. The cavity develops a hemispherical shape while the mass from the droplet is fully attached to the cavity (Fig. 4(c), Fully Attached). Overall, the Liquid Lump, Partially Attached, and Fully Attached cases in the low volume fraction condition show similar trends to those when a water droplet impacts on a water pool as discussed in Appendix C.

Markedly different phenomena are observed at higher ϕ . Fig. 4(d) shows the Wrapped Bubble case, where the cavity becomes unstable soon after the impact (2.7ms) and forms bubbles, while the bottom section of the droplet mass remains undeformed and continues to move down as a lump. The bubbles are wrapped by the top section of the particles and eventually pinch off from the cavity and move along with the particle lump. At even higher ϕ , particles move down as a solid lump with the bottom shape remains unchanged (Fig. 4(e), Solid Lump). Notably, there is minimum cavity formation throughout the impact process, similar to the impact of hydrophilic solid ball on liquid surfaces [61–64].

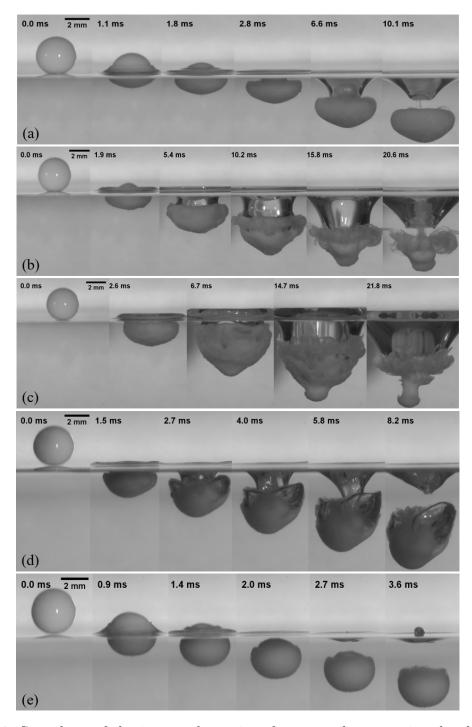


Figure 4: Snapshots of the impact dynamics of cornstarch suspension droplets on a deep water pool. (a) Liquid Lump ($\phi = 36.8\%$, We = 49); (b) Partially Attached ($\phi = 36.8\%$, We = 135); (c) Fully Attached ($\phi = 36.8\%$, We = 290); (d) Wrapped Bubble ($\phi = 41.6\%$, We = 142); (e) Solid Lump ($\phi = 47.5\%$, We = 132)

3.2 Regime map and its physical interpretation

The five phenomena discussed above are mapped in the We- ϕ space, as depicted in Fig. 5. We captures the relative importance between inertia and capillary effects, while ϕ accounts for the rheology of the cornstarch suspension.

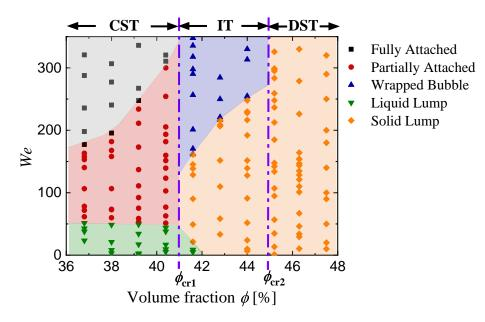


Figure 5: Regime map of impact outcomes of cornstarch suspension droplet on deep water pool in the We- ϕ space. Two dash-dotted lines denote two critical values of volume fraction $\phi_{cr1} = 41\%$ and $\phi_{cr2} = 45\%$ that divide the regime map into three regions of different impact outcomes. ϕ_{cr1} and ϕ_{cr2} equal to the critical volume fractions identified from the rheological data presented in Fig. 2(b). The regime map is thus divided into CST, IT, and DST regions, as denoted on the top of the figure. In each region, We-dependent boundaries can be identified to further divide into different regimes.

First, the regime map can be readily grouped into three regions by two critical volume fractions $\phi_{cr1} = 41\%$ and $\phi_{cr2} = 45\%$, as marked as the dash-dotted lines in Fig. 5. Specifically, at low ϕ ($< \phi_{cr1}$), Liquid Lump, Partially Attached, and Fully Attached as shown in Fig. 4(a)-(c) are observed as We increases. At high ϕ ($> \phi_{cr2}$), only Solid Lump is observed, while both Wrapped Bubble and Solid Lump are observed in the intermediate ϕ range. In each of these regions, We-dependent

transition boundaries between different phenomena can be identified.

Interestingly, ϕ_{cr1} and ϕ_{cr2} agree exactly with those from the rheological characterization (Fig. 2(b)) that grouped the cornstarch suspension into CST, IT, and DST regions. The rheological behavior corroborates well with the qualitative observation of the impact outcome. In the CST region, where the shear thickening behavior is not significant, liquid-like behavior are observed and are similar to water droplet impacts as discussed in Appendix C. At low We, the droplet possesses relatively low initial energy, resulting in a diminished cavity kinetic energy. Therefore, the cavity has limited interactions with the droplet, leading to the Liquid Lump case. As We increases, the cavity obtains larger kinetic energy, allowing it to interact with the merged mass from the droplet. However, the cavity is not fully developed so that only part of cornstarch particles are dispersed, presenting the Partially Attached case. Further increasing We, the cavity has enough kinetic energy to disperse most of the cornstarch particles during the evolution stage of the cavity, giving rise to the Fully Attached case. In the DST region, impacted-activated jamming happens immediately due to its rheological characteristic with large values of α in the power law $\tau_{\eta} \propto \dot{\gamma}^{\alpha}$. Large portion of the droplet mass jams and only a small fraction of top of the droplet mass remains liquid, signified by the vortices as the droplet mass falls. The jamming phenomenon is similar to when a suspension droplet impact on a solid surface [49, 50]. While in the IT region at high We, the bottom part of the droplet mass is jammed as a lump but large part of the top section still remains liquid-like, due to lower α compared to the DST region. The liquid-like top section interacts with the cavity to form bubbles. It should be noted that this bubble formation is caused by the coexisting fluid and solid phases of the merged droplet mass and the interaction between cavity and jammed lump, which is different from the bubble entrapment reported in Newtonian droplet impacting on liquid surfaces [37, 65, 66]. To demonstrate the contribution of the non-Newtonian jamming to the bubble formation instead of merely high viscous effect, glycerol droplet impacting on water surface is tested as an example of high viscous Newtonian fluids. The different features between cornstarch suspension and glycerol droplet is discussed in Appendix D.

To further demonstrate the effect of jamming, deformation of the droplet during the impact process is characterized. The evolution of the normalized droplet height L/D with normalized time $\tau = tu_0/D$ is measured for both low ϕ and high ϕ cases, as shown in Fig. 6. L measures the distance between the top-most point and the bottom-most point of the droplet, as shown in the insets, and is tracked at the early stage of the impact till the moment when the top point of the droplet meets the horizontal level of the liquid surface. At low ϕ , L decreases monotonically, exemplifying the liquid behavior where the top surface keeps flowing under inertia. However, at high ϕ case, L/D plateaus indicating the deformation stops because of jamming, similar to that observed for suspension drop impacting a solid surface [48, 49].

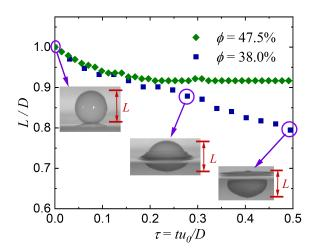


Figure 6: Variation of the normalized height of droplet L/D with normalized time $\tau = tu_0/D$ for low ϕ (= 38.0%) and high ϕ (= 47.5%) both at $u_0 = 1.0$ m/s. The droplet height L, which is marked in the insets, is measured between the moment when the bottom of the droplet contacts the liquid surface (t = 0 ms) and the moment when the top of the droplet meets the horizontal level of the liquid surface.

4 Physical scaling laws of the Transition boundaries

4.1 Energy balance model

To understand and predict the transition boundaries in the regime map, the energy balance during the impact process is analyzed. The general energy balance model is discussed in this section and will be adapted in each regime. For simplicity, the cavity shape is assumed to be hemispherical, as suggested in [67–69]. Prior to the impact, the system energy is comprised of inertial energy $E_{in} = \pi \rho_d D^3 u_0^2 / 12$ and surface energy $E_{sur} = \sigma \pi D^2$ of the droplet. After the impact, the droplet merges with the pool and converts energy to the pool through the cavity in multiple forms. First, the potential energy of the cavity $E_{c,p}$ is the work required to lift the liquid contents of the cavity to the liquid surface due to mass conservation, which can be expressed as $E_{c,p} = \pi \rho_w g R_c^4 / 4$ [67, 69–71], where R_c is the radius of the hemispherical cavity. As the cavity develops, the increased surface area leads to the increase in the surface energy: $E_{c,s} = \sigma(2\pi R_c^2 - \pi R_c^2) = \sigma \pi R_c^2$. In the meanwhile, flow is induced in the pool as the cavity evolves, resulting in the kinetic energy of the cavity $E_{c,k}$. The expression for $E_{c,k}$ based on potential flow theory has been developed in previous studies [67– 69. Due to the complex influence of cornstarch particles on the velocity field in the pool, we incorporate $E_{c,k}$ in subsequent calculations without an explicit expression. Besides the energy conversion to the cavity, the impact also induces internal flow in the droplet which dissipates energy through viscous effect, which can be calculated as

$$E_{\eta} = t^* \int \tau_{\eta} \dot{\gamma} d^3 r \tag{1}$$

where t^* is the characteristic time scale for the impact process, which has distinct values for different regimes and will be calculated individually. The rheology is mod-

eled as $\tau_{\eta} = k(\phi)\dot{\gamma}^{\alpha}$, where the prefactor $k(\phi)$ is a function of volume fraction ϕ and the dependence will be found separately in different regimes. Different values of α are also used for different regions as discussed in Table. 1 and Fig. 2(b). Specifically, averaged value of 1.5 is used for the CST region and $\alpha = 2$ for the IT region. The characteristic shear rate is modeled as $\dot{\gamma} = u_0/D$ [48, 49]. Considering all these energy forms, the energy balance can be written as

$$E_{in} + E_{sur} = E_{c,p} + E_{c,s} + E_{c,k} + E_{\eta} \tag{2}$$

4.2 Transition boundaries in the CST region

4.2.1 Boundary between Liquid Lump and Partially Attached

When the droplet impacts the liquid pool, the droplet energy is partially converted to the pool forming a cavity that moves down. In the meantime, the mass from the droplet penetrates the pool due to inertia. If the cavity has high enough energy, it can catch up with the droplet mass and interact with the particles, thus forming the *Partially Attached* case shown in Fig. 4(b). Otherwise, the particles in the droplet move down without effect from the cavity, as in the *Liquid Lump* case presented in Fig. 4(a). Thus, the cavity energy is crucial for the transition criteria between the *Liquid Lump* and *Partially Attached* cases, which can be characterized by the normalized maximum cavity depth $R_{\text{max}}^* = R_{\text{max}}/D$. Fig. 7 compares R_{max}^* between the *Liquid Lump* and *Partially Attached* cases. By averaging the values of the boundary points, a critical $R_{\text{max},cr}^* = 1.42$ can be identified that separates the two cases. If $R_{\text{max}}^* < 1.42$, *Liquid Lump* points are observed; otherwise, *Partially Attached* points are observed.

The energy balance in Eq. (2) can be carried out to the instant when the cavity reaches the maximum depth to extract the critical We_{cr} for the transition boundary. A few simplifications can be made. Since the expansion velocity of the cavity \dot{R}_c is zero when the cavity reaches the maximum depth, $E_{c,k}$ can be dropped off since

 $E_{c,k} \propto \dot{R}_c$. As shown in Fig. 5, Liquid Lump occurs in the low volume fraction and low impact velocity region. The viscosity of the cornstarch suspension is in the range of 0.02 Pa·s < η_d < 0.04 Pa·s based on the rheological data presented in Fig. 2(a). Re is estimated to be around 200. Thus, viscous dissipation E_{η} can be safely neglected in this region. Thus the energy balance can be simplified as $E_{in} + E_{sur} = E_{c,p} + E_{c,s}$ and can be further organized as follows

$$\frac{We}{12} + 1 = \frac{\rho^* R_{\text{max}}^{*4}}{2l_{c,d}^*} + R_{\text{max}}^{*2} \tag{3}$$

where $\rho^* = \rho_d/\rho_w = 1.635$ is the density ratio between the droplet and the pool, and $l_c^* = \sqrt{2\sigma/\rho_d g}/D \approx 1$ is the normalized capillary length of the droplet. At the transition boundary, $R_{\text{max},cr}^* = 1.42$ as identified in Fig. 7. Substituting these values into Eq. (3), we can find the critical $We_{cr} = 52.08$, which perfectly matches the boundary between $Liquid\ Lump$ and $Partially\ Attached$ cases in regime map shown in Fig. 5. The We_{cr} is a constant independent of the volume fraction, which shows as a horizontal line in Fig. 5.

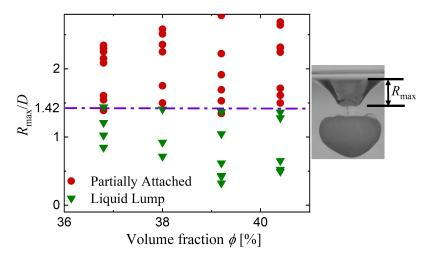


Figure 7: Normalized maximum depth of the cavity $R_{\text{max}}^* = R_{\text{max}}/D$ obtained from the experimental data of the *Liquid Lump* and *Partially Attached* cases. The critical $R_{\text{max},cr}^* = 1.42$ at the boundary of the two cases is independent of ϕ , which is denoted by the horizontal dash-dotted line.

4.2.2 Boundary between Partially Attached and Fully Attached

At even higher We, the cavity has more energy that fully disperses the particles from the droplet, resulting in the Fully Attached case. The energy of the cavity is evaluated at the onset of the cavity evolution stage at t^* . If the cavity kinetic energy $E_{c,k}$ at t^* is above a critical value, it will propagate fast enough to fully disperse the particles as it evolves. t^* is determined when the top surface of droplet catches up with the bottom surface during the initial stage and can be calculated by $D/(u_{top} - u_{bot})$ [72]. u_{top} is the velocity of top surface where $u_{top}/u_0 \approx 1$ at the early stage of the impact due to its liquid nature, and u_{bot} is the velocity of bottom surface, where $u_{bot}/u_0 \approx 0.61$ as shown in Fig. 8(a). Thus $t^* = 5D/2u_0$. The rheology data in Fig. 2(a) indicates that Re is around 70 in this regime, thus the viscous dissipation E_{η} cannot be neglected. Plugging in $t^* = 5D/2u_0$ and $\tau_{\eta} = k(\phi)\dot{\gamma}^{1.5}$ in CST region, viscous dissipation can be expressed as $E_{\eta} = 10\pi D^{1.5}k(\phi)u_0^{1.5}/3$. Therefore, the normalized energy balance equation at $t = t^*$ has the following form

$$\frac{E_{c,k}}{\sigma\pi D^2} = \frac{We}{12} + 1 - \frac{\rho^* R_c^{*4}}{2l_{c,d}^*} - R_c^{*2} - \frac{10k(\phi)u_0^{1.5}}{3\sigma D^{0.5}}$$
(4)

where $R_c^* = R_c/D$ is the normalized radius of the cavity at $t = t^*$ and can be calculated as $R_c^* = u_{bot}t^* = 1.5$. Plugging the values of ρ^* , R_c^* and l_c^* , Eq. (4) can be organized as,

$$\frac{E_{c,k}}{\sigma\pi D^2} = \frac{We}{12} - \frac{10k(\phi)u_0^{1.5}}{3\sigma D^{0.5}} - 0.8$$
 (5)

Here, $k(\phi) = 0.107\phi - 0.037$ is fitted from rheological data in Fig. 2(a) based on $\tau_{\eta} = k(\phi)\dot{\gamma}^{1.5}$, as shown in Fig. 8(b). Fig. 8(c) plots the RHS of Eq. (5) of boundary points in both the *Partially Attached* and *Fully Attached* cases. A critical value of 10.5 can be identified at the transition boundary as indicated by the dashed line. The normalized cavity kinetic energy $E_{c,k}/\sigma\pi D^2$ at the beginning of the evolution stage t^* needs to be larger than 10.5 for the *Fully Attached* case to be observed. The

critical We_{cr} at the transition boundary can thus be calculated by equating the RHS of Eq. (5) to 10.5, which depends on the volume fraction implicitly. Solving for We_{cr} numerically, the theoretical transition boundary is plotted in Fig. 8(d), which shows an excellent agreement with the experimental data. Higher ϕ leads to higher E_{η} , thus requires higher initial energy or We_{cr} for the cavity to retain enough energy to disperse the particles.

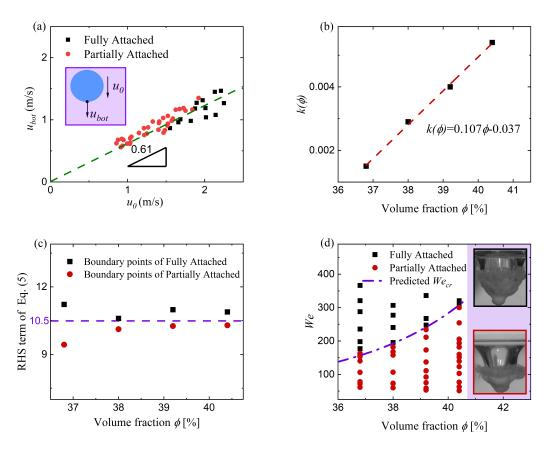


Figure 8: (a) Relationship between velocity of the bottom point of the droplet during the impact process u_{bot} and the impact velocity u_0 . The green dash line has a slope of 0.61, fitted by both Fully Attached data and Partially Attached data. (b) $k(\phi)$ is obtained from the rheological data in Fig. 2(a), based on $\tau_{\eta} = k(\phi)\dot{\gamma}^{\alpha}$ with $\alpha = 1.5$ in the CST region. The red dash line $k(\phi) = 0.107\phi - 0.037$ is linearly fitted from the data. (c) RHS of Eq. (5) at the boundary of Fully Attached and Partially Attached cases as a function of ϕ . A critical value of 10.5 is identified discerning the two phenomena, which is independent of ϕ as denoted by the horizontal dash line. (d) Comparison of the predicted transition boundary with the experimental data for Fully Attached and Partially Attached cases. The theoretical critical Weber number We_{cr} calculated from Eq. (5) is denoted by the dash-dotted line.

4.3 Transition boundary in IT region

Fig. 9 presents the schematic of the energy conversion and transition criteria between $Wrapped\ Bubble$ and $Solid\ Lump$ in the Inertial Transition region. The bottom section of the cornstarch particles jams upon impact on the pool surface, while the top section of the droplet mass is not fully jammed and still presents liquid-like behavior. If the cavity has high enough energy, it keeps expanding and disturbs the unjammed particles. Unlike the $Fully\ Attached$ case, the cavity cannot disperse all the particles since it is blocked by the jammed section. Thus the cavity converts the excess kinetic energy to surface energy to form bubbles. On the other hand, if there is not enough energy for the cavity to expand, no bubble is formed. The transition boundary between $Wrapped\ Bubble$ and $Solid\ Lump$ thus depends on the kinetic energy of the cavity. Specifically, if $E_{c,k}$ is high enough to disperse the top section of the cornstarch particles, the generated cavity interacts with the bottom section of the jammed particles, eventually evolves into bubbles, as shown in Fig. 4(d).

Since only a fraction of the merged droplets remains liquid-like, viscous dissipation happens only in the liquid phase, the percentage of which is denoted by θ . The energy balance can be rewritten as $E_{in} + E_{sur} = E_{c,p} + E_{c,s} + E_{c,k} + \theta E_{\eta}$, and is evaluated from the beginning of the impact to $t^* = D/u_0$. The inertia timescale for the droplet to be fully immersed in the pool [48–50] is adopted, which is different from section 4.2.2 since the top surface cannot catch up with the bottom surface due to jamming in the IT region. Since the energy balance is evaluated at the early stage of the impact, the normalized radius of the cavity $R_c^* = R_c/D \ll 1$. Thus both $E_{c,p}$ and $E_{c,s}$ can be neglected. Furthermore, the rheological properties in the IT region are characterized by $\tau_{\eta} = k(\phi)\dot{\gamma}^{\alpha}$ with $\alpha = 2$, so that the energy dissipation E_{η} in Eq. (1) can be written as $E_{\eta} = \pi D k(\phi) u_0^2/6$. Therefore, the normalized energy balance at $t = t^*$ can be expressed as,

$$\frac{E_{c,k}}{\sigma\pi D^2} = \frac{We}{12} + 1 - \theta \frac{k(\phi)u_0^2}{6\sigma D} \tag{6}$$

where $k(\phi)$ in the IT region cannot be modeled by a linear function as in the CST region. Instead, a classical model $k(\phi) = K(1 - \phi/\phi_{\text{max}})^{\beta}$ [43], which could capture the divergent trend of the viscosity, is adopted as shown in Fig. 10(a). The maximum achievable cornstarch volume fraction for the experiment $\phi_{\text{max}} = 0.52$ as stated in section 2.2 is adopted and $\beta = -7.69$ and $K = 5.3 \times 10^{-9}$ are fitted from the data shown in Fig. 10(a). For simplicity, θ is assumed to be independent of ϕ and u_0 . Thus, θ and $E_{c,k}$ can be simultaneously fitted using the points near the transition boundary between Solid Lump and Wrapped Bubble: $\theta = 0.3$ and $E_{c,k}/\sigma\pi D^2 = 14.7$. $\theta = 0.3$ means that roughly 30% of droplet mass remains as liquid phase, which is reasonable. The critical Weber number We_{cr} can thus be obtained by solving Eq. (6) and is shown as the dash-dotted line in Fig. 10(b). As ϕ increases, higher initial energy or We_{cr} is needed to form Wrapped Bubble. At the same We across the transition boundary, higher ϕ leads to higher $k(\phi)$, resulting in the divergence of droplet viscosity. Thus jamming happens, leading to Solid Lump.

The predicted critical We_{cr} does not agree perfectly with the experimental data. One possible reason is that θ is assumed to be a constant but it can change with varying impact velocity and volume fraction. This detailed variation of θ is complicated and will be investigated further in future research. The prediction of the transition boundary captures the major physics, where $Wrapped\ Bubble$ is a result of a combination of jamming and excess kinetic energy of the cavity.

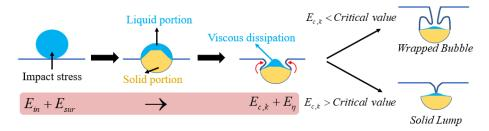


Figure 9: Schematic of the energy balance during the impact process of the cornstarch droplet in the IT region and the criteria to form Wrapped Bubble or Solid Lump. The impact stress induces partial solidification in the droplet resulting in the solid-liquid coexisting phase. Viscous dissipation in the liquid phase leads to reduced cavity kinetic energy $E_{c,k}$. If $E_{c,k}$ is larger than a critical value, the cavity has enough energy to form Wrapped Bubble. Otherwise, there is not enough energy to form the cavity, leading to the Solid Lump case.

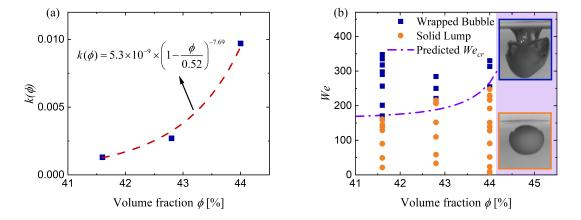


Figure 10: (a) $k(\phi)$ obtained from the rheological data in Fig. 2(a), based on $\tau_{\eta} = k(\phi)\dot{\gamma}^{\alpha}$ with $\alpha = 2$ in the IT region. The red dash line is fitted to capture the divergent behavior. (b) Comparison of the predicted transition boundary with the experimental data for Wrapped Bubble and Solid Lump cases. The theoretical critical Weber number We_{cr} calculated from Eq. (6) is denoted by the dash-dotted line.

5 Conclusion

The impact dynamics of cornstarch suspension droplets on water pool is systematically investigated and characterized with energy balance analysis. Five distinctive phenomena are observed at different regions in the $We-\phi$ regime map. Unique impact dynamics such as $Wrapped\ Bubble$ and $Solid\ Lump$ are observed that are not present for Newtonian droplet. Non-Newtonian effect, especially jamming and the liquid-solid co-existence phase, plays an important role in affecting the impact dynamics. Difference volume fraction dependence of the rheological behavior leads to different interaction between the cavity and particles which is also important in mitigating the dynamics. Energy balance is carried out to predict the transition boundaries, which agree well with the experimental data.

The regime map of the impact outcomes and theoretical prediction of the transition boundaries are summarized in Fig. 11. Two critical volume fractions are identified that divide the regime map into CST, IT, and DST regions, which corroborate well with the rheological measurements. In each region, critical We_{cr} is further predicted with different functional dependence on the volume fraction. In CST region, liquid-like behavior is observed which includes $Liquid\ Lump$, $Partially\ Attached$, and $Fully\ Attached$. In DST region, only $Solid\ Lump$ is observed, while $Wrapped\ Bubble$ is observed at higher We in the IT region. The regime map and predicted transition boundaries lay the systematic foundation for future research on more detailed dynamics for suspension droplet impact on liquid surfaces. It also provides the design guidelines for various applications with specific goals of the impact outcomes.

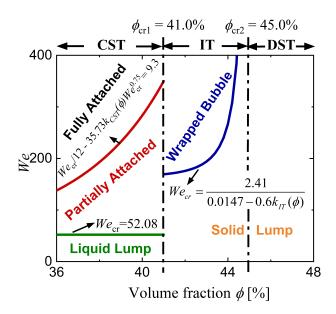


Figure 11: Regime map with predicted scaling laws for the transition boundaries for cornstarch droplet impacting on liquid pool. $k_{CST}(\phi) = 0.107\phi - 0.037$, $k_{IT}(\phi) = 5.3 \times 10^{-9} \times (1 - \phi/0.52)^{-7.69}$.

Appendix A Method for calculating volume fraction of cornstarch suspension

Since cornstarch particles are porous, the following calculation of volume fraction ϕ is adopted [59]:

$$\phi_v = \frac{(1-\beta)m_c/\rho_c}{(1-\beta)m_c/\rho_c + m_w/\rho_w + \beta m_c/\rho_c}$$
(7)

$$\phi = (1 + \alpha)\phi_v \tag{8}$$

where subscript c denotes cornstarch particles and subscript w denotes the base liquid water. In our system, $\rho_c = 1630 \text{ kg/m}^3$, $\rho_w = 997 \text{ kg/m}^3$. α, β are parameters determined by experiments and are recommended that $\alpha = 0.3$, $\beta = 0.11$ [54]. Based on the mass ratio between particles and solvent, the corrected volume fraction could be calculated by Eq. (7) and Eq. (8).

Appendix B Measurement of droplet diameter and impact speed

Fig. 12 shows the measurement of the droplet diameter and impact speed through image analysis. The droplet diameter remains consistent across the range of volume fraction tested in the experiment, as shown in Fig. 12(a). In Fig. 12 (b), different velocities are selected for different volume fractions for clear visualization. The inset shows the log-log plot of the displacement and good linear behavior is observed.

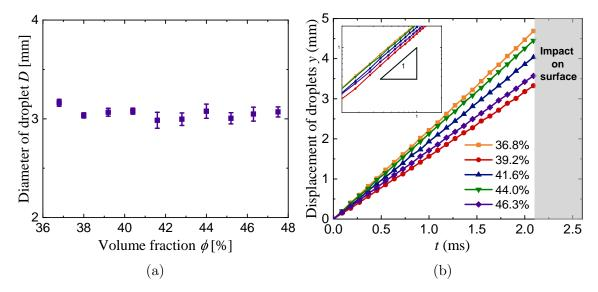


Figure 12: (a) Diameter of the droplet at various volume fractions. (b) Displacement of the centroid of the droplet prior to impact on liquid surface at different volume fractions and impact velocities. Inset shows the log-log plot of the displacement which shows good fitting to the linear trend. In order to provide a clear visualization, different impact velocity cases have been selected for various volume fractions in this figure.

Appendix C Impact of water droplet on water pool

The impact dynamics of water droplet on water pool is shown in Fig. 13 to demonstrate the similar behavior compared to cornstarch droplet impact in the CST region. The shaded regions surrounding the cavity in Fig. 13(a)-(c) represent the dye intentionally introduced in the droplet to track the liquid from the droplet. At low We depicted in Fig. 13(a), the cavity exhibits a relatively small volume, resulting in limited dispersion of the dye, which is similar to the $Liquid\ Lump$ case of cornstarch droplet. As We increases (Fig. 13(b)), the cavity volume is larger and the dye appears in a thin layer. However, at the moment of 11.99 ms, there is still a small portion of dye that remains detached from the cavity. This observation is reminiscent of the phenomena observed in the $Partially\ Attached$ case for cornstarch droplet. As We further increases, the cavity undergoes further development and disperses the dye completely, forming a uniform and continuous thin layer without any detachment. This behavior is akin to the characteristics exhibited in the $Fully\ Attached$ case during the impact of cornstarch droplets.

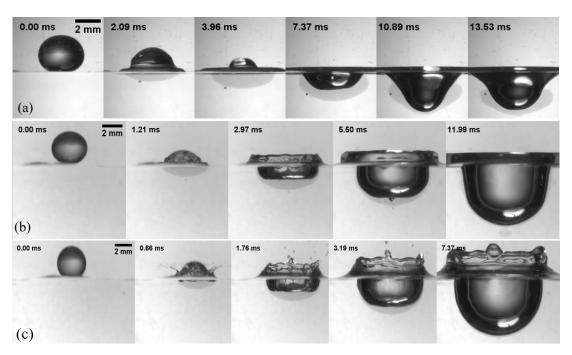


Figure 13: Water droplets impact on water surface. (a) We = 74. (b) We = 157. (c) We = 214.

Appendix D Impact dynamics of glycerol droplet on water pool

The impact dynamics of glycerol droplet on water pool is shown in Fig. 14 to demonstrate the different mechanisms for bubble formation as compared to cornstarch droplet impact. The key distinction is that the surfaces of water pool and glycerol droplet are separated after the impact (Fig. 14(b), 1.10ms), and the surface of pool forms bubble after the separation. However, in the cornstarch droplet impact, the top part of the droplet mass behaves liquid-like, which merges with the surface of the pool and is not detached during the impact process. In the case of the glycerol droplet, noticeable deformation occurs as it transforms into a thin layer, while the surface of the pool undergoes downward motion, resulting in the formation of a substantial cavity. However, in the case of cornstarch droplets, the presence of the jammed section (bottom part) inhibits the expansion of the cavity, leading to the wrapping of two bubbles. It is noteworthy that the occurrence of the Wrapped Bubble case can be observed at much lower We compared to the impact of glycerol droplets. More detailed discussion on the cavity dynamics will be explored in the future work.

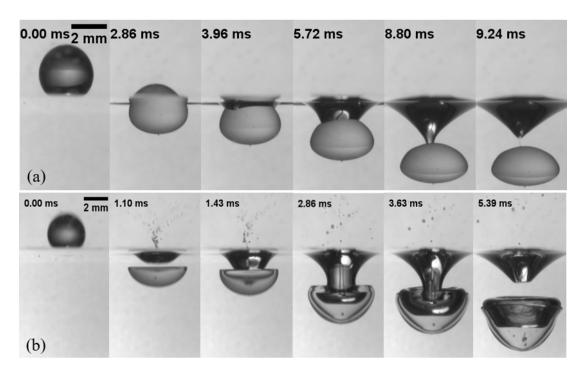


Figure 14: Glycerol droplets impact on water surface. (a) We = 22.11. (b) We = 912.03.

References

- [1] A. L. Yarin, "Drop impact dynamics: splashing, spreading, receding, bouncing.," *Annu. Rev. Fluid Mech.*, vol. 38, pp. 159–192, 2006.
- [2] M. Rein, "Phenomena of liquid drop impact on solid and liquid surfaces," Fluid. Dyn. Res., vol. 12, no. 2, pp. 61–93, 1993.
- [3] K. L. Pan and C. K. Law, "Dynamics of droplet-film collision," *J. Fluid Mech.*, vol. 587, pp. 1–22, 2007.
- [4] Z. Che and O. K. Matar, "Impact of droplets on immiscible liquid films," *Soft Matter*, vol. 14, no. 9, pp. 1540–1551, 2018.
- [5] S. Kim, Z. Wu, E. Esmaili, J. J. Dombroskie, and S. Jung, "How a raindrop gets

- shattered on biological surfaces," *Proc. Natl. Acad. Sci. U.S.A.*, vol. 117, no. 25, pp. 13901–13907, 2020.
- [6] S. Gart, J. E. Mates, C. M. Megaridis, and S. Jung, "Droplet impacting a cantilever: A leaf-raindrop system," *Phys. Rev. Appl.*, vol. 3, no. 4, p. 044019, 2015.
- [7] S. Bagchi, S. Basu, S. Chaudhuri, and A. Saha, "Penetration and secondary atomization of droplets impacted on wet facemasks," *Phys. Rev. Fluid*, vol. 6, no. 11, p. 110510, 2021.
- [8] E. Dressaire, A. Sauret, F. Boulogne, and H. A. Stone, "Drop impact on a flexible fiber," *Soft Matter*, vol. 12, no. 1, pp. 200–208, 2016.
- [9] M. Pack, H. Hu, D. Kim, Z. Zheng, H. Stone, and Y. Sun, "Failure mechanisms of air entrainment in drop impact on lubricated surfaces," *Soft Matter*, vol. 13, no. 12, pp. 2402–2409, 2017.
- [10] P. Tsai, S. Pacheco, C. Pirat, L. Lefferts, and D. Lohse, "Drop impact upon micro-and nanostructured superhydrophobic surfaces," *Langmuir*, vol. 25, no. 20, pp. 12293–12298, 2009.
- [11] M. Guémas, Á. G. Marín, and D. Lohse, "Drop impact experiments of non-newtonian liquids on micro-structured surfaces," Soft Matter, vol. 8, no. 41, pp. 10725–10731, 2012.
- [12] U. Jain, M. Jalaal, D. Lohse, and D. van der Meer, "Deep pool water-impacts of viscous oil droplets," *Soft Matter*, vol. 15, no. 23, pp. 4629–4638, 2019.
- [13] D.-H. Jeong, L. Xing, J.-B. Boutin, and A. Sauret, "Particulate suspension coating of capillary tubes," *Soft Matter.*, vol. 18, no. 42, pp. 8124–8133, 2022.
- [14] M. Singh, H. M. Haverinen, P. Dhagat, and G. E. Jabbour, "Inkjet printing—process and its applications," Adv. Mater., vol. 22, no. 6, pp. 673–685, 2010.

- [15] B. Mohan, W. Yang, and S. kiang Chou, "Fuel injection strategies for performance improvement and emissions reduction in compression ignition engines—a review," Renew. Sust. Energ. Rev., vol. 28, pp. 664–676, 2013.
- [16] D. Richard, C. Clanet, and D. Quéré, "Contact time of a bouncing drop," Nature, vol. 417, no. 6891, pp. 811–811, 2002.
- [17] J. de Ruiter, R. Lagraauw, D. van den Ende, and F. Mugele, "Wettability-independent bouncing on flat surfaces mediated by thin air films," *Nat. Phys.*, vol. 11, no. 1, pp. 48–53, 2015.
- [18] J. M. Kolinski, L. Mahadevan, and S. M. Rubinstein, "Drops can bounce from perfectly hydrophilic surfaces," *EPL*, vol. 108, no. 2, p. 24001, 2014.
- [19] X. Tang, A. Saha, C. K. Law, and C. Sun, "Bouncing-to-merging transition in drop impact on liquid film: Role of liquid viscosity," *Langmuir*, vol. 34, no. 8, pp. 2654–2662, 2018.
- [20] J. Zou, P. F. Wang, T. R. Zhang, X. Fu, and X. Ruan, "Experimental study of a drop bouncing on a liquid surface," *Phys. Fluids*, vol. 23, no. 4, p. 044101, 2011.
- [21] Z. He, H. Tran, and M. Y. Pack, "Drop bouncing dynamics on ultrathin films," Langmuir, vol. 37, no. 33, pp. 10135–10142, 2021.
- [22] J. Lee, N. Laan, K. G. de Bruin, G. Skantzaris, N. Shahidzadeh, D. Derome, J. Carmeliet, and D. Bonn, "Universal rescaling of drop impact on smooth and rough surfaces," J. Fluid Mech., vol. 786, p. R4, 2016.
- [23] G. Lagubeau, M. A. Fontelos, C. Josserand, A. Maurel, V. Pagneux, and P. Petitjeans, "Spreading dynamics of drop impacts," J. Fluid Mech., vol. 713, pp. 50–60, 2012.

- [24] I. V. Roisman, R. Rioboo, and C. Tropea, "Normal impact of a liquid drop on a dry surface: model for spreading and receding," *Philos. Trans. Royal Soc. A*, vol. 458, no. 2022, pp. 1411–1430, 2002.
- [25] N. Laan, K. G. de Bruin, D. Bartolo, C. Josserand, and D. Bonn, "Maximum diameter of impacting liquid droplets," Phys. Rev. Appl., vol. 2, no. 4, p. 044018, 2014.
- [26] S. Wildeman, C. W. Visser, C. Sun, and D. Lohse, "On the spreading of impacting drops," *J. Fluid Mech.*, vol. 805, pp. 636–655, 2016.
- [27] X. Tang, A. Saha, C. Sun, and C. K. Law, "Spreading and oscillation dynamics of drop impacting liquid film," J. Fluid Mech, vol. 881, pp. 859–871, 2019.
- [28] M. Mani, S. Mandre, and M. P. Brenner, "Events before droplet splashing on a solid surface," *J. Fluid Mech.*, vol. 647, pp. 163–185, 2010.
- [29] L. Xu, W. W. Zhang, and S. R. Nagel, "Drop splashing on a dry smooth surface," Phys. Rev. Lett., vol. 94, no. 18, p. 184505, 2005.
- [30] L. V. Zhang, P. Brunet, J. Eggers, and R. D. Deegan, "Wavelength selection in the crown splash," *Phys. Fluids*, vol. 22, no. 12, p. 122105, 2010.
- [31] D. W. Murphy, C. Li, V. d'Albignac, D. Morra, and J. Katz, "Splash behaviour and oily marine aerosol production by raindrops impacting oil slicks," *J. Fluid Mech.*, vol. 780, pp. 536–577, 2015.
- [32] L. Yang, Z. Li, T. Yang, Y. Chi, and P. Zhang, "Experimental study on droplet splash and receding breakup on a smooth surface at atmospheric pressure," *Lang-muir*, vol. 37, no. 36, pp. 10838–10848, 2021.
- [33] G. Juarez, T. Gastopoulos, Y. Zhang, M. L. Siegel, and P. E. Arratia, "Splash control of drop impacts with geometric targets," *Phys. Rev. E*, vol. 85, no. 2, p. 026319, 2012.

- [34] X. Peng, T. Wang, K. Sun, and Z. Che, "Droplet splashing during the impact on liquid pools of shear-thinning fluids with yield stress," *Phys. Fluids*, vol. 33, no. 11, p. 112106, 2021.
- [35] T. Tran, H. de Maleprade, C. Sun, and D. Lohse, "Air entrainment during impact of droplets on liquid surfaces," *J. Fluid Mech.*, vol. 726, p. R3, 2013.
- [36] S. T. Thoroddsen, M.-J. Thoraval, K. Takehara, and T. Etoh, "Micro-bubble morphologies following drop impacts onto a pool surface," J. Fluid Mech., vol. 708, pp. 469–479, 2012.
- [37] W. Bouwhuis, R. C. van der Veen, T. Tran, D. L. Keij, K. G. Winkels, I. R. Peters, D. van der Meer, C. Sun, J. H. Snoeijer, and D. Lohse, "Maximal air bubble entrainment at liquid-drop impact," *Phys. Rev. Lett.*, vol. 109, no. 26, p. 264501, 2012.
- [38] M. A. Quetzeri-Santiago, K. Yokoi, A. A. Castrejón-Pita, and J. R. Castrejón-Pita, "Role of the dynamic contact angle on splashing," *Phys. Rev. Lett.*, vol. 122, no. 22, p. 228001, 2019.
- [39] R. C. van der Veen, T. Tran, D. Lohse, and C. Sun, "Direct measurements of air layer profiles under impacting droplets using high-speed color interferometry," *Phys. Rev. E*, vol. 85, no. 2, p. 026315, 2012.
- [40] P. D. Hicks and R. Purvis, "Air cushioning in droplet impacts with liquid layers and other droplets," *Phys. Fluids*, vol. 23, no. 6, p. 062104, 2011.
- [41] X. Tang, A. Saha, C. K. Law, and C. Sun, "Bouncing drop on liquid film: Dynamics of interfacial gas layer," *Phys. Fluids*, vol. 31, no. 1, p. 013304, 2019.
- [42] C. Josserand and S. T. Thoroddsen, "Drop impact on a solid surface," *Annu. Rev. Fluid Mech.*, vol. 48, pp. 365–391, 2016.

- [43] J. Mewis and N. J. Wagner, *Colloidal suspension rheology*. Cambridge university press, 2012.
- [44] J. F. Morris, "Toward a fluid mechanics of suspensions," *Phys. Rev. Fluids.*, vol. 5, no. 11, p. 110519, 2020.
- [45] D. Bi, J. Zhang, B. Chakraborty, and R. P. Behringer, "Jamming by shear," Nature, vol. 480, no. 7377, pp. 355–358, 2011.
- [46] M. Krüger, "Properties of non-equilibrium states: Dense colloidal suspensions under steady shearing," *Colloids*, 2009.
- [47] S. Butler and P. Harrowell, "The shear induced disordering transition in a colloidal crystal: Nonequilibrium brownian dynamic simulations," J. Chem. Phys., vol. 103, no. 11, pp. 4653–4671, 1995.
- [48] F. Boyer, J. H. Snoeijer, J. F. Dijksman, and D. Lohse, "Drop impact of shear thickening liquids," *Phys. Rev. Fluid*, vol. 1, no. 1, 2016.
- [49] P. Shah, S. Arora, and M. M. Driscoll, "Coexistence of solid and liquid phases in shear jammed colloidal drops," *Commun. Phys.*, vol. 5, no. 1, p. 222, 2022.
- [50] P. Shah and M. M. Driscoll, "Drop impact dynamics of complex fluids: A review," 2021.
- [51] L. Jørgensen, Y. Forterre, and H. Lhuissier, "Deformation upon impact of a concentrated suspension drop," *J. Fluid Mech.*, vol. 896, p. R2, 2020.
- [52] A. Fall, F. Bertrand, G. Ovarlez, and D. Bonn, "Shear thickening of cornstarch suspensions," *J. Rheol.*, vol. 56, no. 3, pp. 145–150, 2012.
- [53] R. I. Tanner, "Review article: Aspects of non-colloidal suspension rheology," Phys. Fluids, vol. 30, no. 10, 2018.

- [54] E. Han, N. V. Ha, and H. M. Jaeger, "Measuring the porosity and compressibility of liquid-suspended porous particles using ultrasound," Soft Matter, vol. 13, no. 19, 2017.
- [55] E. Brown and H. M. Jaeger, "Shear thickening in concentrated suspensions: phenomenology, mechanisms and relations to jamming," Rep. Prog. Phys., vol. 77, no. 4, p. 046602, 2014.
- [56] C. E. Stauffer, "The measurement of surface tension by the pendant drop technique," *J. Phys. Chem.*, vol. 69, 1965.
- [57] E. Y. Arashiro and N. R. Demarquette, "Use of the pendant drop method to measure interfacial tension between molten polymers," *Mater. Res.*, vol. 2, pp. 23–32, 1999.
- [58] S. R. Waitukaitis and H. M. Jaeger, "Impact-activated solidification of dense suspensions via dynamic jamming fronts," *Nature*, vol. 487, no. 7406, pp. 205– 209, 2012.
- [59] E. Han, I. R. Peters, and H. M. Jaeger, "High-speed ultrasound imaging in dense suspensions reveals impact-activated solidification due to dynamic shear jamming," *Nat. Commun.*, vol. 7, no. 1, p. 12243, 2016.
- [60] E. Guazzelli and J. F. Morris, A physical introduction to suspension dynamics, vol. 45. Cambridge University Press, 2011.
- [61] C. Duez, C. Ybert, C. Clanet, and L. Bocquet, "Making a splash with water repellency," *Nat. Phys.*, vol. 3, no. 3, pp. 180–183, 2007.
- [62] T. T. Truscott, B. P. Epps, and J. Belden, "Water entry of projectiles," Annu. Rev. Fluid Mech., vol. 46, pp. 355–378, 2014.
- [63] J. M. Aristoff, T. T. Truscott, A. H. Techet, and J. W. Bush, "The water entry of decelerating spheres," *Phys. Fluids*, vol. 22, no. 3, p. 032102, 2010.

- [64] H. Marschall, K. A. Mørch, A. Keller, and M. Kjeldsen, "Cavitation inception by almost spherical solid particles in water," *Phys. Fluids*, vol. 15, no. 2, pp. 545– 553, 2003.
- [65] Q. Deng, A. Anilkumar, and T. Wang, "The role of viscosity and surface tension in bubble entrapment during drop impact onto a deep liquid pool," J. Fluid Mech., vol. 578, pp. 119–138, 2007.
- [66] V. Mehdi-Nejad, J. Mostaghimi, and S. Chandra, "Air bubble entrapment under an impacting droplet," *Phys. Fluids.*, vol. 15, no. 1, pp. 173–183, 2003.
- [67] V. Lherm, R. Deguen, T. Alboussière, and M. Landeau, "Rayleigh-taylor instability in impact cratering experiments," *J. Fluid Mech*, vol. 937, p. A20, 2022.
- [68] X. Tang, A. Saha, C. K. Law, and C. Sun, "Nonmonotonic response of drop impacting on liquid film: mechanism and scaling," Soft Matter, vol. 12, no. 20, pp. 4521–4529, 2016.
- [69] A. I. Fedorchenko and A.-B. Wang, "On some common features of drop impact on liquid surfaces," *Phys. Fluids*, vol. 16, no. 5, pp. 1349–1365, 2004.
- [70] O. G. Engel, "Crater depth in fluid impacts," J. Appl. Phys., vol. 37, no. 4, pp. 1798–1808, 1966.
- [71] H. Lamb, *Hydrodynamics*. University Press, 1924.
- [72] A. Bisighini, G. E. Cossali, C. Tropea, and I. V. Roisman, "Crater evolution after the impact of a drop onto a semi-infinite liquid target," *Phys. Rev. E.*, vol. 82, no. 3, p. 036319, 2010.